Vol. 40 (2009) *ACTA PHYSICA POLONICA B* No 2

VERTICAL OSCILLATIONS OF A CURVED CORONAL SLAB IN AN INHOMOGENEOUS PLASMA

M. Gruszecki, K. Murawski

Group of Astrophysics and Gravity Theory, Institute of Physics, UMCS
Radziszewskiego 10, 20-031 Lublin, Poland

S. Fromang, R. Teyssier

Service d'Astrophysique, CEA/DSM/DAPNIA/SAp, Centre d'Études de Saclay
91191 Gif-sur-Yvette Cedex, France

(Received October 8, 2008)

The influence of a few different Alfvén speed profiles $V_{\mathrm{A}}(z)$ on the development of vertical oscillations of a curved coronal slab is investigated. Three particular cases are discussed: (a) $dV_{\mathrm{A}}/dz < 0$, (b) $dV_{\mathrm{A}}/dz = 0$, (c) $dV_{\mathrm{A}}/dz > 0$. These cases correspond respectively to the presence of wave tunnelling into the ambient medium above the slab (a), lack of any tunnelling (b), and tunnelling into the ambient medium below the slab (c). Two-dimensional ideal magnetohydrodynamic equations are solved by numerical means and the slab oscillations are triggered impulsively by an initial pulse in the vertical component of the momentum. We find that vertical oscillations exhibit time-signatures with characteristic wave period P and attenuation time τ. These parameters vary with $V_{\mathrm{A}}(z)$. A smallest value of P is associated with the case of (c). A strongest attenuation (smallest τ) of vertical oscillations takes place in the case of (a). A simple model of coronal loop oscillations leads to numerical results which are akin to the observational data of Wang and Solanki (2004).

PACS numbers: 95.30.Qd, 96.60.Hv, 96.60.P–, 96.60.Ly

1. Introduction

Waves and oscillations of a solar coronal loop is a topic of recent intensive investigations (*e.g.* Smith *et al.* 1997; del Zanna *et al.* 2005; Murawski *et al.* 2005; Selwa *et al.* 2006; Verwichte *et al.* 2006a,b,c; Diáz *et al.* 2006; Gruszecki *et al.* 2006; Ofman 2007). The general conclusion drawn from these investigations is that a coronal loop is able to sustain a cavity either for propagating or standing waves (Edwin and Roberts 1982). Among standing waves several modes are possible to distinguish. Hot loops are observed to oscillate mainly in a slow magnetoacoustic mode (Wang *et al.* 2002). Cool loops primarily oscillate in fast magnetoacoustic kink modes which are observed in two polarizations: horizontal (Aschwanden *et al.* 1999; Nakariakov *et al.* 1999; Van Doorsselaere *et al.* 2007) and vertical (Wang and Solanki 2004). An excellent review of these oscillations can be found in Nakariakov and Verwichte (2005).

The role of different Alfvén speed profiles on the behaviour of magnetohydrodynamic waves in a coronal loop was already addressed in the literature. For instance, Smith *et al.* (1997) studied the leakage of fast magnetoacoustic sausage and kink oscillations with exponentially decreasing Alfvén speed profile. Brady and Arber (2005) discussed higher-order ($n \geq 5$) fast magnetoacoustic kink modes in a semi-circle coronal loop and explained the leakage as wave tunnelling through an evanescent barrier above the coronal loop. Recently, Verwichte *et al.* (2006a,b,c) developed an analytical model for vertically polarised fast magnetoacoustic waves in a curved coronal loop. In Verwichte *et al.* (2006a) the coronal loop was modeled in the limit of cold plasma approximation as a curved magnetic slab for equilibrium mass density given by a piece-wise continuous power law profile. Depending on this profile, the wave modes were trapped or they were all subject to lateral wave leakage (upward or downward). Verwichte *et al.* (2006b) confirmed that vertically polarised fast magnetoacoustic kink oscillations of isolated coronal loops may be efficiently attenuated due to lateral leakage. Verwichte *et al.* (2006c) concluded that the mechanism of lateral wave leakage was efficient in attenuation of vertically polarised fast kink oscillations.

Of particular importance to this paper is the work by Brady and Arber (2005) and Verwichte *et al.* (2006b), who investigated fast magnetoacoustic waves in curved coronal loops and the role of lateral leakage in wave attenuation, which includes the mechanism of wave tunnelling. However, Verwichte *et al.* (2006b) considered the case of plasma beta $\beta = 2\mu p/\vec{B}^2 = 0$ for a current loop while we extend their model for the case of warm plasma ($\beta \neq 0$) and introduce a current-free potential arcade loop model. Brady and Arber (2005) discussed the case of a finite-value of β. However, they limited their discussion to higher-order modes, while we concentrate our attention on fundamental vertical kink loop oscillation. As a result, our approach is complementary to the work by Brady and Arber (2005) and Verwichte *et al.* (2006b).

This paper is organised as follows: The numerical model is described in Sect. 2. The numerical results are presented in Sect. 3. Here we explore the effects of different parameters entering the problem. The conclusions are given in Sect. 4.

2. Setup

2.1. Magnetohydrodynamic equations and numerical methods

We perform numerical simulations in a two-dimensional magnetically structured atmosphere. Henceforth, we neglect gravity, thermal conduction, radiation, plasma heating, viscosity and resistivity. As a consequence of that we use the ideal magnetohydrodynamic equations to describe the coronal plasma:

$$\frac{\partial \varrho}{\partial t} + \nabla \cdot (\varrho \boldsymbol{V}) = 0\,, \tag{1}$$

$$\varrho \frac{\partial \boldsymbol{V}}{\partial t} + \varrho\,(\boldsymbol{V} \cdot \nabla)\,\boldsymbol{V} = -\nabla p + \frac{1}{\mu}(\nabla \times \boldsymbol{B}) \times \boldsymbol{B}\,, \tag{2}$$

$$\frac{\partial p}{\partial t} + \boldsymbol{V} \cdot \nabla p = -\gamma p \nabla \cdot \boldsymbol{V}\,, \tag{3}$$

$$\frac{\partial \boldsymbol{B}}{\partial t} = \nabla \times (\boldsymbol{V} \times \boldsymbol{B})\,, \tag{4}$$

$$\nabla \cdot \boldsymbol{B} = 0\,. \tag{5}$$

Here $\gamma = 5/3$ is the adiabatic index, μ is the magnetic permeability, ϱ is the mass density, $\boldsymbol{V}$ is the flow velocity, p is the gas pressure and $\boldsymbol{B}$ is the magnetic field.

Equations (1)–(5) are solved numerically using the code `RAMSES` (Teyssier 2002; Fromang *et al.* 2006). This code implements a second-order unsplit Godunov solver with various slope limiters and Riemann solvers as well as Adaptive Mesh Refinement (AMR). We use the Monotonized Central slope limiter and the HLLD Riemann solver (*e.g.* Toro 1999). We set the simulation box as $(0, 2\,L) \times (0, 2\,L)$, with $L = 100$ Mm. Open boundary conditions for all perturbed plasma quantities are imposed in the two spatial directions. In our studies we use AMR grid with a minimum (maximum) level of refinement set to 5 (10). The refinement strategy is based on controlling numerical errors in mass density. This results in an excellent resolution of steep spatial profiles and greatly reduces numerical diffusion at these locations. Initially (at $t = 0$) we cover the simulation region by 10^6 numerical cells.

2.2. Initial setup

In this section, we detail the initial setup used in this paper. The corona is modeled as a low mass density, current free, highly magnetized plasma laying over a dense photosphere. A dense curved slab is embedded in the corona.

2.2.1. The structure of the atmosphere

In this model, we assume that the gas pressure, p_{e}, is initially uniform. The boundary between the photosphere and the corona is chosen to lay at the reference level, $z = z_{\mathrm{ph}} = 0.4\,L$. If we neglect the effect of gravity, the mass density can then be selected arbitrarily in the entire computational domain. In particular we implement

$$\varrho_{\mathrm{e}}(z) = \varrho_{\mathrm{c}}(z) + \frac{1}{2}\varrho_{\mathrm{c}}(z)(d_{\mathrm{ph}} - 1)\left[1 - \tanh\left(\frac{z - z_{\mathrm{ph}}}{s_{\mathrm{ph}}}\right)\right] . \tag{6}$$

Here

$$\varrho_{\mathrm{c}}(z) = \hat{\varrho}_{\mathrm{c}} \exp\left(-\frac{z - z_{\mathrm{ph}}}{\Lambda_{\mathrm{c}}}\right) , \tag{7}$$

where Λ_{c} is the mass density scale height and $\hat{\varrho}_{\mathrm{c}}$ denotes the mass density at $z = z_{\mathrm{ph}}$. The subscript e denotes the equilibrium mass density, s_{ph} is the width of the transition region that is located at $z = z_{\mathrm{ph}}$ and d_{ph} is the ratio of the mass density of the photosphere to the ambient coronal medium. In this paper, we choose and hold fixed $s_{\mathrm{ph}} = 1$ Mm and $d_{\mathrm{ph}} = 10^3$ (Gruszecki *et al.* 2008).

For the initial magnetic field, we adopt and modify the magnetic field model which was originally described by Priest (1982) and recently used by Gruszecki *et al.* (2008). In this model, we assume that at the equilibrium the coronal arcade is embedded in a two-dimensional space. We limit our discussion to a case of current-free magnetic field $\nabla \times \vec{B}_{\mathrm{e}} = 0$ and introduce the magnetic potential

$$A(x, z) = B_0 \Lambda_{\mathrm{B}} \cos\left(x/\Lambda_{\mathrm{B}}\right)\exp[-(z - z_{\mathrm{ph}})/\Lambda_{\mathrm{B}}] . \tag{8}$$

It is related to the magnetic field through $\vec{B}_{\mathrm{e}} = \nabla \times (A\hat{\boldsymbol{y}})$. The equilibrium magnetic field components $(B_{\mathrm{ex}}, B_{\mathrm{ez}})$ are then given by

$$(B_{\mathrm{ex}}, B_{\mathrm{ez}}) = B_0(\cos x/\Lambda_{\mathrm{B}}, -\sin x/\Lambda_{\mathrm{B}})\exp[-(z - z_{\mathrm{ph}})/\Lambda_{\mathrm{B}}] , \tag{9}$$

in addition to $B_{\mathrm{ey}} = 0$. Here B_0 is the magnetic field at $z = z_{\mathrm{ph}}$ and the magnetic scale height is $\Lambda_{\mathrm{B}} = 2\pi/L$.

2.2.2. The curved mass density slab

We implement a dense curved slab in the solar corona. It is established such that its edges follow specific magnetic field lines. This can be done by implementing the following mass density profile in the coronal region:

$$\varrho_{\mathrm{s}}(x, z) = \varrho_{\mathrm{c}}(z) + \tfrac{1}{2}(d - 1)\varrho_{\mathrm{c}}(z) f(x, y) , \tag{10}$$

where the function $f(x,y)$ is defined for $z \geq z_{\rm ph}$ as

$$f(x,y) = \left| \mathrm{erf}\left(\frac{A(x,z)-A_1}{B_0\Lambda_{\rm B}}\right) - \mathrm{erf}\left(\frac{A(x,z)-A_2}{B_0\Lambda_{\rm B}}\right) \right| . \tag{11}$$

Here $A_1 = A(x_1,0) > A_2 = A(x_1+2a_{\rm f},0)$ and erf is the error function. The symbol x_1 corresponds to the external left slab footpoint and $a_{\rm f}$ denotes the half-width of the slab at $z = z_{\rm ph}$. We set $x_1/L = 0.3$ and $a_{\rm f}/L = 0.025$. This slab embraces a region of enhanced mass density plasma with a mass density contrast $d = \varrho_{\rm i}(z)/\varrho_{\rm c}(z) = 10$ (Aschwanden and Nightingale 2005), where $\varrho_{\rm i}(z)$ and $\varrho_{\rm c}(z)$ respectively stands for the mass density of the curved slab and that of the local ambient coronal plasma.

Note that for the above choice of parameters, the curved slab does not have a circular shape (see Fig. 1): the average radius and length are respectively ~ 70 Mm and ~ 190 Mm. These values are close to the observational data of Wang and Solanki (2004). In this paper, we choose $\hat{c}_{\rm s} = \sqrt{\gamma p_{\rm e}/\hat{\varrho}_{\rm c}} = 2\times 10^5$ ms^{-1} for the sound speed and $\hat{V}_{\rm A} = B_0/\sqrt{\mu\hat{\varrho}_{\rm c}} = 10^6$ ms^{-1} for the Alfvén speed at $z = z_{\rm ph}$. For such a choice, we find $\beta = 2\hat{c}_{\rm s}^2/(\gamma\hat{V}_{\rm A}^2) = 0.012$, which is a realistic value in the corona.

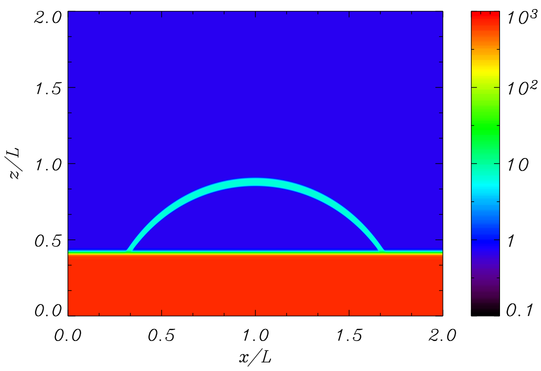

Fig. 1. Initial equilibrium mass density profile in the x–z plane. The dense photosphere-like layer is located at $z/L < 0.4$.

With the above choice of magnetic field and mass density profiles, the Alfvén speed in the solar corona is given by:

$$V_{\rm A}(z) = \frac{B_{\rm e}(z)}{\sqrt{\mu\varrho_{\rm c}(z)}} = \sqrt{\frac{B_0^2}{\mu\varrho_{\rm c}}\exp\left(\frac{(1-2\Lambda_{\rm c}/\Lambda_{\rm B})(z-z_{\rm ph})}{\Lambda_{\rm c}}\right)} . \tag{12}$$

By varying the ratio $\Lambda_{\rm c}/\Lambda_{\rm B}$, we can vary the vertical slope of the Alfvén speed profile. As a magnetic field cannot be measured directly in the solar corona, the Alfvén speed profile is not known there. We can imagine that there are different V_{A} profiles and therefore in this paper, we compared six models for which $\Lambda_{\mathrm{c}}/\Lambda_{\mathrm{B}} = 0.43, 0.47, 0.5, 0.53, 0.63$ and 0.67. In the first two, $dV_{\mathrm{A}}/dz > 0$. In the third model, $dV_{\mathrm{A}}/dz = 0$. Finally, in the last three models, $dV_{\mathrm{A}}/dz < 0$. Figure 2 illustrates the resulting vertical profiles of $V_{\mathrm{A}}(z)$ in the cases $\Lambda_{\mathrm{c}}/\Lambda_{\mathrm{B}} = 0.63$ (dotted line), $\Lambda_{\mathrm{c}}/\Lambda_{\mathrm{B}} = 0.5$ (solid line) and $\Lambda_{\mathrm{c}}/\Lambda_{\mathrm{B}} = 0.43$ (dashed line).

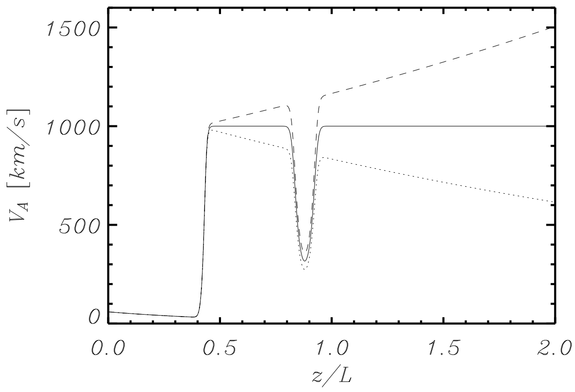

Fig. 2. Vertical profiles of the Alfvén speed for the cases $\Lambda_{\mathrm{c}}/\Lambda_{\mathrm{B}} = 0.63$ (dotted line), 0.5 (solid line) and 0.43 (dashed line). They correspond respectively to $dV_{\mathrm{A}}/dz < 0$, $dV_{\mathrm{A}}/dz = 0$ and $dV_{\mathrm{A}}/dz > 0$.

In this paper, we aim to study impulsively excited fast magnetoacoustic kink oscillations in the curved coronal slab that is described above. These oscillations are triggered by an initial pulse in the vertical component of the momentum (Gruszecki *et al.* 2008)

$$\varrho_{\mathrm{e}}(z)V_z(x,z,t=0) = A_{\mathrm{p}} \exp\left[-\frac{(x-x_0)^2+(z-z_0)^2}{w^2}\right], \qquad (13)$$

where A_{p} is the amplitude of the initial pulse and w is its width. We set $z_0 = z_{\mathrm{ph}}$ (the pulse originates at the base of the corona), $x_0/L = 1$ (the symmetry in the x-direction is preserved) and $w/L = 0.35$ for all cases. Finally, we set $A_{\mathrm{p}} = 0.242\,\hat{V}_{\mathrm{A}}\,\hat{\varrho}_{\mathrm{c}}$.

3. Numerical results

3.1. Basic flow features

For all the simulations, the momentum pulse excited at $t = 0$ s at the base of the corona triggers essentially fast magnetoacoustic waves. Vertical oscillations of the dense curved slab are then excited as this pulse reaches a location of the slab. Figure 3 shows the time-signatures of these oscillations by plotting the evolution of vertical profile of the mass density with time near the curved slab summit. The left, middle and right panels correspond respectively to $\Lambda_c/\Lambda_B = 0.63, 0.5$ and 0.67. These time-signatures reveal apex oscillations that decay with time.

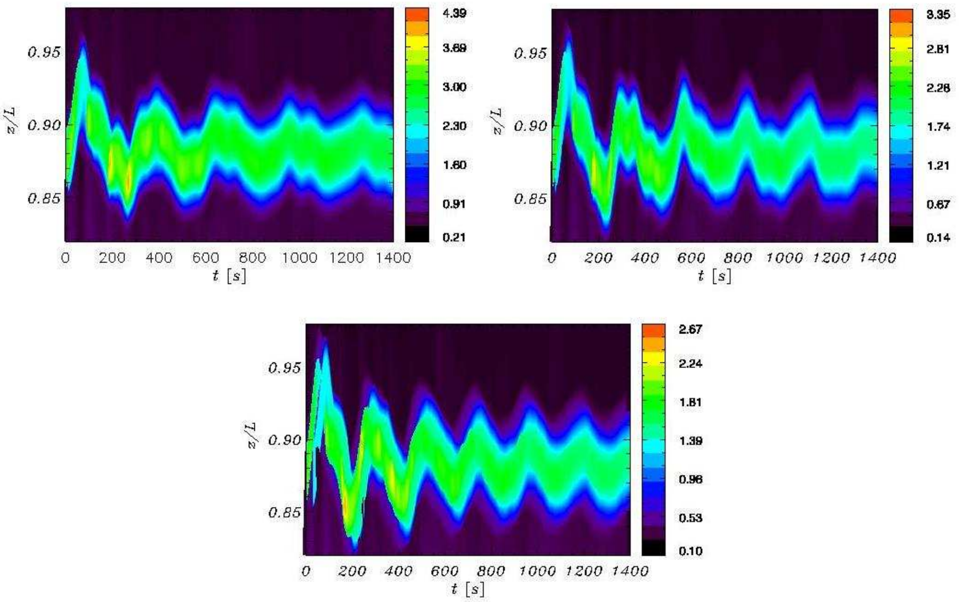

Fig. 3. Time-signatures of mass density, evaluated at $x/L = 1$. Left panel corresponds to $\Lambda_c/\Lambda_B = 0.63$ ($dV_A/dz < 0$), the middle panel to $\Lambda_c/\Lambda_B = 0.5$ ($dV_A/dz = 0$) and right panel to $\Lambda_c/\Lambda_B = 0.67$ ($dV_A/dz > 0$).

For all the models, we plot in Fig. 4 the maximum of the vertical shift of the slab apex z_m *versus* $V_{At} = V_A(z/L = 2)$. It is clear that z_m grows with V_{At}. This growing trend results from the fact that for a larger value of V_{At} wave tunnelling into the ambient corona above the apex is less effective for a flatter descending V_A profile or it is absent for $dV_A/dz \geq 0$. In a case of $dV_A/dz > 0$ wave tunnelling takes place to the medium below the apex. As a result more energy is trapped below the slab and the apex is shifted more substantially upwards. It is noteworthy that within the considered range of V_{At}, we get 4.6 Mm $< z_m < 6$ Mm, which is close to the observational data of 7.9 Mm (Wang and Solanki 2004).

The slab oscillations can be traced by following the position of the slab apex in time. This position is estimated from Fig. 3 as the maximum of the Gaussian function fitted across the slab at its apex. To estimate the wave period P and attenuation time τ of the oscillation, we fit the following

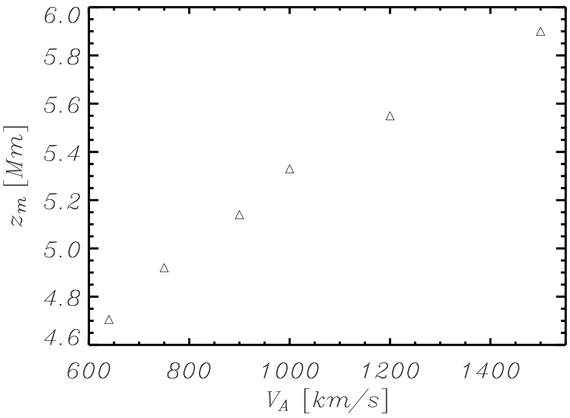

Fig. 4. Maximum of vertical shift of the slab (z_{m}) *versus* $V_{\mathrm{A}}(z/L = 2)$.

attenuated sine function:

$$D(t) = D_0 + D_1 \cdot \sin(D_2 t + D_3) \exp(-D_4 t), \tag{14}$$

to the corresponding position of the slab apex for each model (*e.g.* Gruszecki *et al.* 2008). The wave period and attenuation time of the oscillations are related to the parameters of the fit through $P = 2\pi/D_2$ and $\tau = 1/D_4$. Figure 5 displays the variation of the wave period P with V_{At}. We found

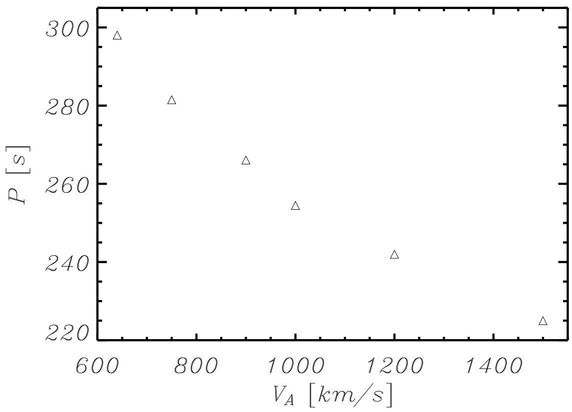

Fig. 5. Plot of the wave period, P, *versus* $V_{\mathrm{A}}(z/L = 2)$.

that P declines with V_{At}. This trend can be qualitatively understood by an analogy with the straight slab (Gruszecki *et al.* 2007). In this case, the wave period of the first magnetosonic kink mode can be estimated from:

$$P \simeq \frac{2l}{\bar{V}_{\mathrm{A}}}, \tag{15}$$

where l is the initial length of the loop and $\bar{V}_{\rm A}$ is the average Alfvén speed within the loop. As this speed grows with $V_{\rm At}$, P is expected to decline with $V_{\rm At}$, which is in a qualitative agreement with the results of Fig. 5.

3.2. Wave tunnelling

3.2.1. Simulations results

The oscillations of the dense curved slab are attenuated because waves tunnel into the ambient corona (Verwichte *et al.* 2006b). The amount of attenuation depends on the thickness of the tunnelling region. The thicker it is, the weaker wave leakage into the corona is, and the longer it will take for the slab oscillations to attenuate. The thickness of the tunnelling region depends on the Alfvén velocity vertical profile. This thickness is infinite for the case of $V_{\rm A}$ = const. as wave tunnelling is absent there. For $dV_{\rm A}/dz < 0$ wave tunnelling takes place into the top ambient corona and the thickness is smaller for a flatter $V_{\rm A}(z)$ profile (a larger value of $V_{\rm At}$). For a case of $dV_{\rm A}/dz > 0$, for which $V_{\rm At}$ attains a larger value than for a case of $dV_{\rm A}/dz < 0$, a larger value of τ/P results from the fact that P declines with $V_{\rm At}$ (Fig. 5). Thus, we expect longer attenuation timescales for a larger value of $V_{\rm At}$. As shown in Fig. 6, it is indeed the case. The quality signal, τ/P, grows with $V_{\rm At}$, supporting our claims. As an additional confirmation, we computed the time-averaged kinetic energy of magnetoacoustic waves, $\bar{E}_{\rm k}$, in a region located just above the curved slab apex ($0.979 < z/L < 1$). We found that $\bar{E}_{\rm k}\left(V_{\rm At} = 1500 \ {\rm km\,s^{-1}}\right) \simeq 0.57\ \bar{E}_{\rm k}(V_{\rm At} = 640\ {\rm km\,s^{-1}})$. This indicates that energy leakage is higher for the case of $V_{\rm At} = 640\ {\rm km\,s^{-1}}$ than for $V_{\rm At} = 1500\ {\rm km\,s^{-1}}$. We infer that energy leakage into the top ambient corona is more substantial for a lower value of $V_{\rm At}$.

3.2.2. Comparison with observations and analytical results

It is noteworthy that the numerically obtained values of τ/P (Fig. 6) are consistent with the observational data of Wang and Solanki (2004), which exhibits a value of $\tau/P \simeq 3$.

The trend obtained in Fig. 6 also agrees qualitatively with the analytical findings of Verwichte *et al.* (2006b). This can be seen for example in their Fig. 10, bottom panel. For ascending ($dV_{\rm A}/dz > 0$) Alfvén speed profile, the values we obtained are even in good quantitative agreement with the values of τ/P quoted in Verwichte *et al.* (2006b). For descending ($dV_{\rm A}/dz < 0$) and constant ($dV_{\rm A}/dz = 0$) Alfvén speed profiles, Verwichte *et al.* (2006b) found that $0.2 < \tau/P < 0.9$. This is smaller by a factor of at least two than exhibited by our numerical simulations.

First, it is worth noting that a one to one comparison is difficult, as Verwichte *et al.* (2006b) adopted the zero-β plasma limit approximation, while we placed the curved slab in the $\beta \neq 0$ corona. Second, the differences are

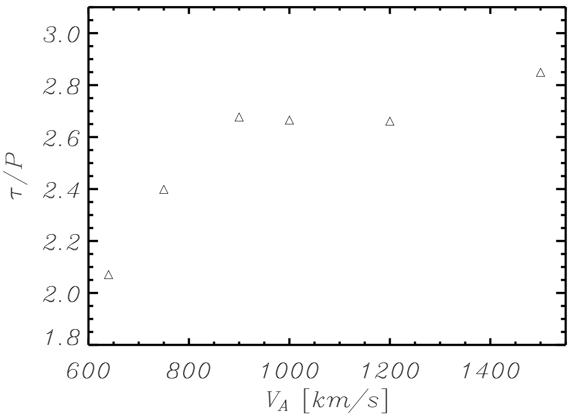

Fig. 6. Ratio of the attenuation time to the wave period, τ/P, *versus* $V_{\rm A}(z/L = 2)$.

also likely to be due to the different Alfvén speed profiles we used compared to Verwichte *et al.* (2006b). Another difference is that the curved slab is akin to a half-ring in Verwichte *et al.* (2006b) while in our case it is oval. As a result the apex is shifted further up than in our case (Fig. 4).

4. Summary

In this paper, we presented a parametric study of the influence of the vertical profile of the Alfvén speed on the spatial and temporal evolution of vertical oscillations of a curved coronal slab. In particular, we discussed descending ($dV_{\rm A}/dz < 0$), constant ($dV_{\rm A}/dz = 0$) and ascending ($dV_{\rm A}/dz > 0$) Alfvén speed profiles. Our findings can be summarised as follows. The initial pulse of momentum imposed at the start of the simulation triggers vertical oscillations that exhibit leakage into a photosphere-like layer (Gruszecki *et al.* 2008) and into the ambient medium. The latter results from curvature of magnetic field lines (Selwa *et al.* 2007) as well as from wave tunnelling into the top and bottom ambient corona (Verwichte *et al.* 2006b) which is present respectively for descending and ascending with height Alfvén speed profiles.

The numerical results obtained in this paper are in good agreement with the observational data of Wang and Solanki (2004) who reported $P = 234$ s and $\tau/P \simeq 3$. We found P in the range 220–300 s and $\tau/P \sim 2.85$ in the case of an ascending Alfvén velocity profile.

Thus we have shown that, even in the absence of thermal conduction, radiation, plasma heating, viscosity or any other non-ideal effects, a simple conceivable model of coronal loop oscillations gives acceptable results, with wave periods and quality signals that are in good agreement with the observational data.

M.G.'s and K.M.'s work was supported by the grant for years 2007–2010 from the Polish Ministry of Science and Higher Education.

REFERENCES

M.J. Aschwanden, L. Fletcher, C.J. Schrijver, D. Alexander, *Astrophys. J.* **520**, 880 (1999).

M.J. Aschwanden, R.W. Nightingale, *Astrophys. J.* **633**, 499 (2005).

C.S. Brady, T.D. Arber, *Astron. Astrophys.* **438**, 733 (2005).

L. del Zanna, E. Schaekens, M. Velli, *Astron. Astrophys.* **431**, 1095 (2005).

A.J. Diáz, R. Oliver, J.L. Ballester, *Astrophys. J.* **645**, 766 (2006).

P.M. Edwin, B. Roberts, *Sol. Phys.* **76**, 239 (1982).

S. Fromang, P. Hennebelle, R. Teyssier, *Astron. Astrophys.* **457**, 371 (2006).

M. Gruszecki, K. Murawski, M. Selwa, L. Ofman, *Astron. Astrophys.* **460**, 887 (2006).

M. Gruszecki, K. Murawski, J.A. McLaughlin, *Astron. Astrophys.* **488**, 757 (2008).

K. Murawski, M. Selwa, J.A. Rossmanith, *Sol. Phys.* **231**, 87 (2005).

V.M. Nakariakov, L. Ofman, E.E. Deluca, B. Roberts, J.M. Davila, *Science* **285**, 862 (1999).

V.M. Nakariakov, E. Verwichte, *Living Rev. Sol. Phys.* **2**, 3 (2005).

L. Ofman, *Astrophys. J.* **655**, 1134 (2007).

E.R. Priest, *Solar Magnetohydrodynamics*, ed. D. Reidel, Dordrecht 1982.

M. Selwa, S.K. Solanki, K. Murawski, T.J. Wang, U. Shumlak, *Astron. Astrophys.* **454**, 653 (2006).

M. Selwa, K. Murawski, S.K. Solanki, T.J. Wang, *Astron. Astrophys.* **462**, 1127 (2007).

J.M. Smith, B. Roberts, R. Oliver, *Astron. Astrophys.* **327**, 377 (1997).

R. Teyssier, *Astron. Astrophys.* 385 **337**, (2002).

E. Toro, *Riemann Solvers and Numerical Methods for Fluid Dynamics*, Springer, Berlin 1999.

T. Van Doorsselaere, V.M. Nakariakov, E. Verwichte, *Astron. Astrophys.* **1051**, 6361 (2007).

E. Verwichte, C. Foullon, V.M. Nakariakov, *Astron. Astrophys.* **446**, 1139 (2006a).

E. Verwichte, C. Foullon, V.M. Nakariakov, *Astron. Astrophys.* **449**, 769 (2006b).

E. Verwichte, C. Foullon, V.M. Nakariakov, *Astron. Astrophys.* **452**, 615 (2006c).

T.J. Wang, S.K. Solanki, W. Curdt, D.E. Innes, I.E. Dammasch, *Astron. Astrophys.* **188**, 199 (2002).

T.J. Wang, S.K. Solanki, *Astron. Astrophys.* **421**, L33 (2004).